Three-dimensional modeling for complex structures based on small-angle X-ray scattering

Tomoyuki Iwata*

Abstract

Three-dimensional real-space modeling for hierarchical materials by matching experimental and simulated small-angle X-ray scattering patterns is proposed. The positional arrangements of small primary particles in the cell are estimated by the reverse Monte Carlo modeling and the simulated SAXS patterns are derived from these models. This modeling has been applied to the structural estimation of a silica aerogel sample. The pore size distribution derived from the obtained structure model is compared to the results of the transmission electron microscopy and gas adsorption measurement.

1. Introduction

Certain functional materials—including catalyst supports[1–3], hybrid polymer composites[4], high-performance rubber tires[5–7], aerogels[8] and so forth—have a hierarchical, nano-scale structure. These structures are composed of complex formations of atomic or nanoparticle-scale primary particles. Transmission and scanning electron microscopy (TEM and SEM, respectively) are commonly used as tools to investigate the precise structure; however, they are not suitable for the investigation of structures that are easily destroyed during sample preparation or for non-conductive materials (insulators). On the other hand, the X-ray scattering method can used for non-destructive analysis of structures with a size ranging from sub-nanometers to sub-micrometers, where the X-rays can penetrate through functional materials without any sample preparation.

Small-angle X-ray scattering (SAXS) is widely used to analyze the shape and size distribution of structures in the nanometer region[9]. In addition, Hasmy *et al*. developed structure factor modeling based on real-space numerical simulation, which was applied to the investigation of aerogels[10,11]. They reported that their simulated patterns exhibit oscillatory fringes corresponding to the single size (diameter) of the primary particles. In general, experimental scattering patterns have no such fringes because a real physical system is polydisperse. Therefore, a precise comparison between the experimental and simulated SAXS patterns could not be performed without introducing polydispersity of the primary particles (distribution of particles size). In this article, we will introduce a novel approach to build a structural model that consists of spherically shape particles having polydispersity in a cubic cell. It assumes a spherical shape for the particles, for the sake of simplicity, and introduces a size distribution in order to fit the experimental SAXS patterns. Particle positions, composed by the model, are randomly moved and evaluated using reverse Monte Carlo (RMC) modeling[12, 13]. Simulated SAXS intensities from the model before and after any changes from the random movement of particles are compared to the experimental data to decide whether a particular model change is accepted or rejected, as judged by improvements in the error. The procedure is repeated until the error converges to a certain level.

The X-ray scattering intensity in electron units of the scattering vector $\vec{q}=\overrightarrow{k_{out}}-\overrightarrow{k_{in}}$ ($\overrightarrow{k_{in}}$ and $\overrightarrow{k_{out}}$ are the wavevectors of the incident and scattered X-rays, respectively) for a system composed of N individual particles is calculated from the following equation[14]:

$$I(\vec{q})=\sum_{m}^{N}\sum_{n}^{N}F_m(\vec{q})F_n(\vec{q})\exp\left(-i\vec{q}\cdot\left(\overrightarrow{r_n}-\overrightarrow{r_m}\right)\right), \quad (1)$$

where $F_m(\vec{q})$ and $F_n(\vec{q})$ are the form factors of the m-th and n-th particles, and $\overrightarrow{r_m}$ and $\overrightarrow{r_n}$ are the positional vectors of the m-th and n-th particles, respectively. If we assume an isotropic system and average the orientation of $\vec{q}$, then equation (1) can be written as a function of $q=|\vec{q}|$,

$$I(q)=\sum_{m}^{N}\sum_{n}^{N}F_m(q)F_n(q)\mathrm{sinc}(qr_{mn}), \quad (2)$$

where r_{mn} is the inter-particle distance ($r_{mn}=|\overrightarrow{r_m}-\overrightarrow{r_n}|$), and $\mathrm{sinc}(x)$ is the unnormalized sinc function ($\mathrm{sinc}(x)=(\sin x)/x$). Equation (2) is the so-called "Debye scattering equation" (DSE)[15].

DSE is so well known that a special issue of *Acta Crystallographica* Section A was published to celebrate its 100th anniversary[16]. It is possible to calculate the scattering intensity of a hierarchical structure from the DSE as long as we put the particles into real space. However, it has been found that the calculated intensities from the DSE are much higher than the experimental data in the low-q regime due to the form factor (shape) of a finite cell size: the periods of low-q fringes are

* X-ray Research Laboratory, Rigaku Corporation.

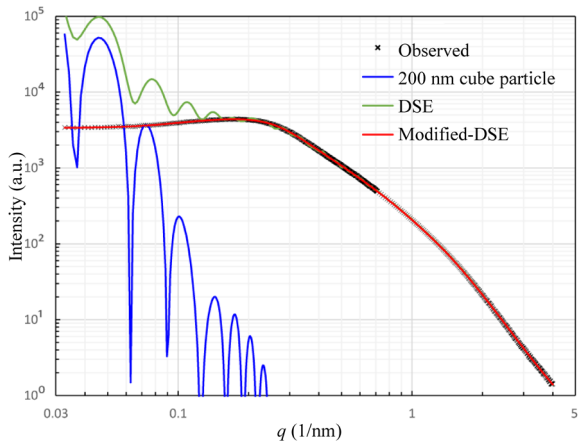

Fig. 1. SAXS patterns: observed intensity data of a silica aerogel sample (× marks) and simulated patterns of the structural model, which has 34,983 particles in the 200 nm cell, by calculating in the DSE (green line) and in a modified-DSE (red line). The calculated pattern of the 200 nm cube is also shown as the blue line.

similar to those of a cubic particle. The former is the green line in Fig. 1 and the latter is the blue line. This cell-size effect for simulated patterns in the low-q regime is a serious problem for investigating the complex structures of composite materials that are several tens of nanometers in size because the small angle scattering pattern in this region has an essential role in determining those structures. Of course, a real system is much larger than a few hundred nanometer correlations and no fringes are observed in real experimental scattering patterns. A simple solution to avoid such unphysical behavior is to increase the size of cell. However, increasing the size of the cell drastically increases the computational cost as follows. When the cell size of a model that contains N particles is increased by A times, the volume of the model increases by A^3 times and the number of the particles in the model, N, also increases by A^3 times. Due to having double summations in the DSE, the calculation cost is disadvantageously increased by A^6 times. Additionally, in the intensity calculation, increasing the number of particles and the cell volume leads to an excessively large number of iterations while repositioning particles in the RMC modeling. As a result, the computational cost of SAXS-RMC modeling is too high to perform on a personal computer. Therefore, simulation in this field requires using a supercomputer such as the Earth simulator (JAMSTEC) and the K computer (RIKEN)[17), 18)].

Recently, we have successfully simulated experimental SAXS patterns of a silica aerogel using RMC modeling that was modified for a finite-size cell[19)] of over a few hundred nanometers. In the next section, we describe the details of our RMC modeling modifications. Then, we will present an approach to analyze the three-dimensional pore size distribution from the obtained structural model, since aerogels have many nanometer-sized pores consisting of loosely packed particles[20)] that exhibit ultralow density and large specific surface area. Finally, the pore size distribution of the obtained structure model is compared to the results of the TEM and the gas adsorption data.

2. Simulation of X-ray Scattering Intensity Based on the Real-space Structure

2.1. Modification of the DSE

Equation (2) can be divided into two cases, one in which the distance r_{mn} is shorter than L and the other where r_{mn} is equal to or longer:

$$I(q)=\sum_{m}^{N}\sum_{n\in r_{mn}<L}^{N}F_m(q)F_n(q)\mathrm{sinc}(qr_{mn}) + \sum_{m}^{N}\sum_{n\in r_{mn}\geq L}^{N}F_m(q)F_n(q)\mathrm{sinc}(qr_{mn}). \quad (3)$$

We will now focus on the second term on the right side of equation (3). When L satisfies the condition that there are many particle pairs in the same distance range around r_{mn}, we assume that the individual form factor can be replaced with the mean value $F^2_{\mathrm{ave}}(q)\equiv\{\sum_m^N\sum_n^N F_m(q)\,F_n(q)\}/N^2$ in this term:

$$\sum_{m}^{N}\sum_{n\in r_{mn}\geq L}^{N}F_m(q)F_n(q)\mathrm{sinc}(qr_{mn}) \approx F^2_{\mathrm{ave}}(q)\sum_{m}^{N}\sum_{n\in r_{mn}\geq L}^{N}\mathrm{sinc}(qr_{mn}). \quad (4)$$

When we introduce the number density $\rho_m(r_{mn})$ of the particles at a distance r_{mn} relative to the m-th particle, the summation over n-th particle in equation (4) can be replaced by an integral:

$$F^2_{\mathrm{ave}}(q)\sum_{m}^{N}\sum_{n\in r_{mn}\geq L}^{N}\mathrm{sinc}(qr_{mn}) = NF^2_{\mathrm{ave}}(q)\sum_{m}^{N}\int_{L}^{\infty}4\pi r^2\rho_m(r_{mn})\mathrm{sinc}(qr_{mn})\,dr. \quad (5)$$

Additionally, averaging $\rho_m(r_{mn})$ for all particles m, $\rho(r)\equiv\{\sum_m^N\rho_m(r_{mn})\}/N$, equation (3) is re-written as:

$$I(q)=\sum_{m}^{N}\sum_{n\in r_{mn}<L}^{N}F_m(q)F_n(q)\mathrm{sinc}(qr_{mn}) + N^2F^2_{\mathrm{ave}}(q)\int_{L}^{\infty}4\pi r^2\rho(r)\mathrm{sinc}(qr)\,dr. \quad (6)$$

Owing to the finite integration range with respect to r in equation (6), the simulated SAXS pattern shows an oscillation in the low-q regime, as shown in Fig. 1. Therefore, we have extended the integration range of r to infinity by assuming an appropriate value $\rho(r)$. The purpose of the simulation for the SAXS pattern is to investigate density fluctuations in the specimen. When the integration is performed between r and $r+dr$, in a case in which the volume is sufficiently

large, $\rho(r)$ can be considered to have a constant value ρ_{ave}, corresponding to the bulk density. This means that the size of the simulation cell must be large enough to satisfy $\rho(r \approx L_{out}) \approx \rho_{ave}$, where L_{out} is half the cell size. Introducing ρ_{ave} to integrate outside of the cell, the integration term of equation (6) can be divided into two parts (inner/outer) as follows:

$$I(q) = \sum_{m}^{N} \sum_{n \in r_{mn} < L}^{N} F_m(q) F_n(q) \operatorname{sinc}(q r_{mn}) + 4\pi N^2 F_{ave}^2(q) \int_{L}^{L_{out}} r^2 \rho(r) \operatorname{sinc}(qr)\, dr + 4\pi N^2 F_{ave}^2(q) \rho_{ave} \int_{L_{out}}^{\infty} r^2 \operatorname{sinc}(qr)\, dr. \quad (7)$$

To fit the experimental SAXS pattern, we also must take into account for the resolution of the instrument. When the resolution is isotropic and has the same value in any azimuthal direction, equation (1) can be modified by the convolution of the divergent $\vec{q}$ vector as follows:

$$\begin{aligned} I(\vec{q}) &= \left[\frac{1}{\sqrt{2\pi}\Delta q} \right]^3 \int \sum_{m}^{N} \sum_{n}^{N} F_m(\vec{q}') F_n(\vec{q}') \exp \\ &\quad \times \left(-i\vec{q}' \cdot \overrightarrow{r_{mn}} \right) \exp \left[-\frac{\left(\vec{q}' - \vec{q} \right)^2}{2\Delta q^2} \right] d\vec{q}' \\ &= \sum_{m}^{N} \sum_{n}^{N} F_m(\vec{q}) F_n(\vec{q}) \exp \\ &\quad \times \left(-i\vec{q} \cdot \overrightarrow{r_{mn}} \right) \exp \left(-\frac{\Delta q^2 r_{mn}^2}{2} \right). \end{aligned} \quad (8)$$

For this derivation, we assume that the form factor of the primary particle varies slowly in the low-q region and $F_m(\vec{q}) \approx F_m(\vec{q}')$ during the integration. In the case of a practical SAXS instrument using a two-dimensional detector, the resolution is limited by the beam size on the detector, δ_D, and camera length, L_C. The maximum angular resolution of the system is δ_D / L_C and is estimated to be

$$\Delta q = \frac{\pi}{\lambda} \frac{\delta_D}{L_C}, \quad (9)$$

where λ is the X-ray wavelength. Then, substituting equation (8) for equation (7), we finally obtain

$$H(q,r) \equiv \operatorname{sinc}(qr) \exp \left(-\frac{\Delta q^2 r^2}{2} \right), \quad (10)$$

$$I(q) = \sum_{m}^{N} \sum_{n \in r_{mn} < L}^{N} F_m(q) F_n(q) H(q, r_{mn}) + 4\pi N^2 F_{ave}^2(q) \int_{L}^{L_{out}} r^2 \rho(r) H(q,r)\, dr + 4\pi N^2 F_{ave}^2(q) \rho_{ave} \int_{L_{out}}^{\infty} r^2 H(q,r)\, dr. \quad (11)$$

Hereinafter, equation (11) is called the "modified-DSE" in this article. The third term expands the integration range of r to infinity. It is noted that the modified-DSE is free from the low-q regime problem. When the modified-DSE is applied to the data of a silica aerogel, the simulated patterns are in reasonably good agreement with the corresponding experimental data (Fig. 1).

2.2. Structural modeling of a silica aerogel

Aerogels, known to be one of the lowest-density solid materials, have attracted attention as thermal insulators with very low thermal conductivity (15 mW/m/K[21]). They are synthesized materials derived from wet gels in which the liquid component of the gel has been replaced with a gas by a special drying technique (such as supercritical drying, ambient pressure drying or freeze drying), without significant collapse of the gel structure. As a result, they contains many nanometer-sized pores consisting of loosely packed particles[20]. Because the air in the pores cannot move smoothly, convection is suppressed. In addition, because the solid framework represents a small portion of the material, they are ineffective for heat conduction[22]–[29]. These physical properties are closely related to the structural features of the primary units and their internal network structures. However, TEM and SEM are not suitable to investigate the entire three-dimensional structure of these materials because they can measure only very thin samples (or the surface of the samples), and depth information may be destroyed during sample preparation. Unfortunately, aerogels are easily shattered like glass by mechanical shock. Therefore, non-destructive analysis using SAXS (and neutron scattering) studies has been extensively performed by many authors[30], [31].

In order to investigate structures having a complex formation of primary particles by SAXS, fractal dimension analysis often has been discussed[32] and the structures have been characterized by the slopes of the SAXS patterns in specific q regimes[33],[34]. These approaches are simple, and they are useful for categorizing structural features related to synthesis conditions and physical properties. However, they only give a qualitative approach. It is difficult to evaluate the physical properties of the objects quantitatively. Therefore, the purpose of this article is to estimate three-dimensional structural models composed of primary particles that are fitted to experimental SAXS patterns on the basis of RMC modeling.

SAXS intensity data of a silica aerogel (SP-30; JFCC, Japan) was collected using a high-performance semiconductor detector (Rigaku HyPix-6000) on a laboratory SAXS measurement system (Rigaku NANOPIX). X-rays from a high-brilliance point-focus X-ray source (Rigaku MicroMax-007 HFMR) were focused and collimated with a multilayer confocal mirror (Rigaku OptiSAXS™) and low parasitic scattering pinhole slits (Rigaku ClearPinhole™). The SAXS pattern was collected in transmission geometry without any sample treatment. The resolution Δq of

the instrument was 0.0064 nm^{-1}. The specimen was sheetlike with a thickness of 1 mm.

To create an initial model, we need two kinds of primary-particle parameters: the particle size distribution and the volume fraction in the simulated cell. Particle size distribution parameters were determined from the observed pattern in the high-q regime ($2.8 < q < 4.3\,nm^{-1}$) using the Rigaku analysis software NANO-Solver. The average diameter of the primary particle was found to be 2.7 nm, and the coefficient of variation was 0.28 under the assumption that the particle size distribution was a gamma function. The bulk density of the specimen was estimated to be 0.123 $g\,cm^{-3}$ by comparing the X-ray absorption of the specimen with that of a reference (amorphous silica, 2.2 $g\,cm^{-3}$). The volume fraction of the primary particles was 5.6 vol%. The derived particle size distribution and the volume fraction were introduced to set the weight function of a particle-radius random number generator and the limit of the particle total volume in the cell, respectively. According to these conditions, the total numbers of primary particles, N, were set to be 4,381, 34,983 and 117,846 for simulation cell sizes of 100 nm, 200 nm and 300 nm, respectively. An additional assumption was to avoid particle-particle duplications during the simulation. The goodness-of-fit between the simulation and the experimental data is defined by using the weight function w_i as follows:

$$\begin{cases} w_{i>0} \equiv \ln q_{i-1} - \ln q_i \\ w_0 = w_1 \end{cases}, \tag{12}$$

$$\chi^2 = \frac{\sum_i w_i \left[\ln I_{\mathrm{Exp}}(q_i) - \ln I_{\mathrm{Sim}}(q_i) \right]^2}{\sum_i w_i \left[\ln I_{\mathrm{Exp}}(q_i) \right]^2}, \tag{13}$$

where $I_{\mathrm{Exp}}(q_i)$ and $I_{\mathrm{Sim}}(q_i)$ are the experimental and simulated scattering intensities, respectively, at wavenumber q_i. Each MC iteration proceeds as follows. 1) randomly select particles and modify their positions, 2) evaluate the goodness-of-fit, χ', after the movement, 3) compare this value with the value before the movement χ. If $\chi' < \chi$, then the model including the modified positions is accepted.

The resultant three-dimensional structural model reproduces the experimental SAXS pattern well, as shown in Fig. 2. The simulated intensity in the low-q regime ($q < 0.5\,nm^{-1}$) has increased about ten times from that of the initial structure where primary particles are randomly positioned (Fig. 2(a)). This suggests that the large-scale structures are successfully configured by rearranging the positions of the primary particles in order to fit the experimental SAXS pattern. However, it should be noted that, for the cell size of 100 nm, there are small deviations from the experimental SAXS pattern in Fig. 2(b), which shows an enlargement of Fig. 2(a) in the low-q ($< 0.5\,nm^{-1}$) regime. This is also seen in the graph of the density function $\rho(r)$ shown in Fig. 3, where the result for the 100 nm cell is a little different

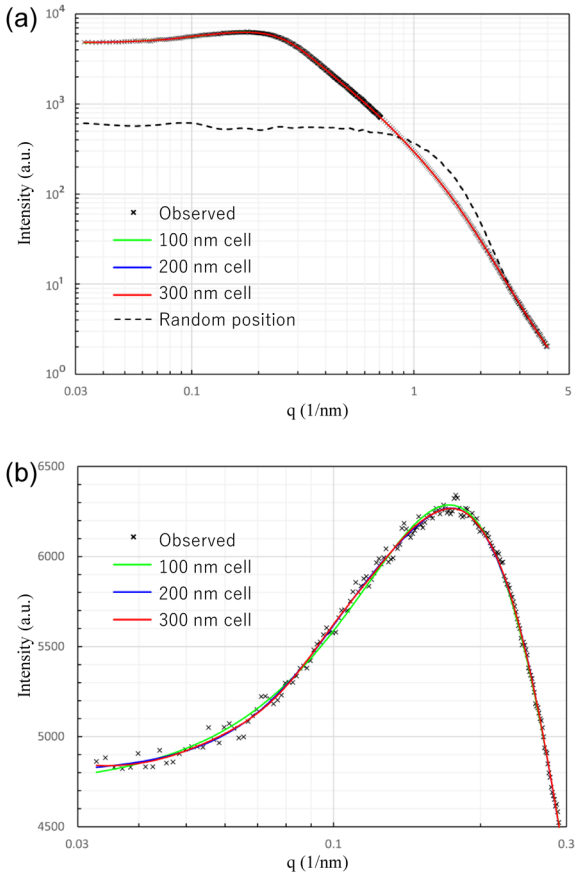

Fig. 2. SAXS patterns (a) all q regime and (b) enlarged $q < 0.3\,nm^{-1}$ regime. Observed intensity data of a silica aerogel sample (× marks), simulated patterns of the RMC modeling (100 nm cell = green line, 200 nm cell = blue line, and 300 nm cell = red line). The calculated pattern from the randomly positioned primary particles is also shown in (a) (black dashed line).

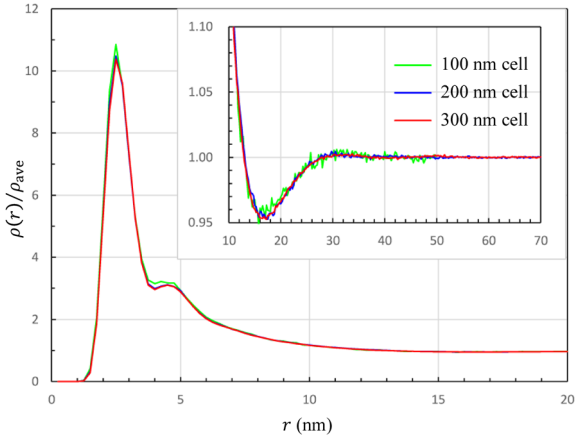

Fig. 3. The normalized density distribution of the primary particles.

from those obtained with cell sizes of 200 and 300 nm. This suggests that the preferred cell size is 200 nm or more for simulated silica aerogel structure modeling matched to collected SAXS data. In the next section, we introduce quantitative analysis of the pore size

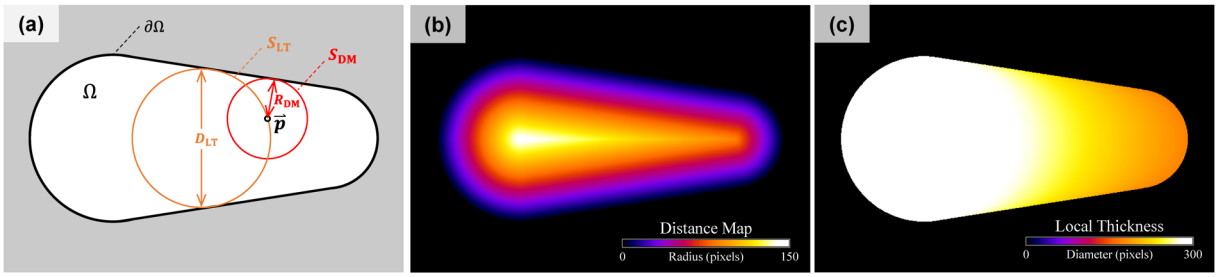

Fig. 4. Illustrations of the binary picture transformation.
(a) Source binary picture with a target object Ω and assigned spheres when we calculate grid-point values at the point $\vec{p}$, those spheres S_{DM} and S_{LT} are for the transformations in the distance map (DM) and the local thickness (LT), respectively.
Computational transformation results, (b) for the DM and (c) for the LT, are shown as the color maps.

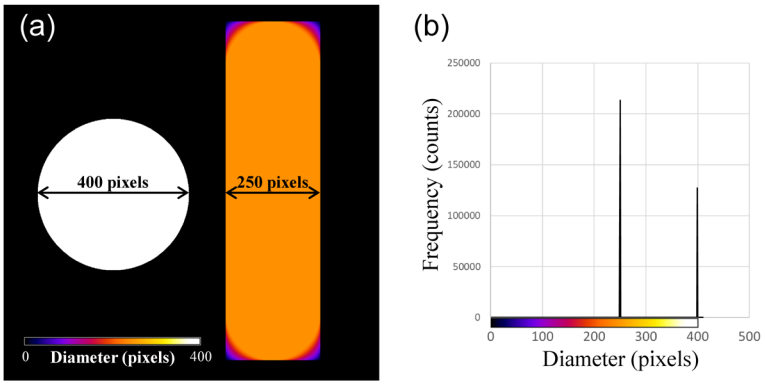

Fig. 5. Local thickness (LT) transformation results of a ball and a stick.
(a) a color map and (b) histogram.

distribution for comparing the results of the obtained structure model based on the experimental SAXS data with TEM and gas adsorption.

3. Characterization of the Pore Size Distribution

In this section, we have analyzed the structural features in the obtained three-dimensional model. Many types of analyses for such complex structures have been developed, mainly for three-dimensional structures obtained by computed tomography (CT)[35)–(39)]. First, the observed image is transformed to binary data that assigns grid point values (GPV) to their pixels; for example, an inside object is set to 0 and an outside object set to 1. The Euclidean distance map (DM)[40), (41)] can be calculated by the distance transformation from the original binary GPV. Mathematically, when we characterize the object (pore) Ω as shown in Fig. 4(a), GPV of DM at a point of $\vec{p}$ inside Ω is calculated by

$$R_{DM}(\vec{p}) = \min(\{d(\vec{p}, \vec{x}) | \vec{x} \in \partial\Omega\}), \quad (14)$$

where $d(\vec{p}, \vec{x})$ is the Euclidean distance between $\vec{p}$ and $\vec{x}$, $\partial\Omega$ is the surface of Ω, and $\vec{x} \in \partial\Omega$ is a grid point in $\partial\Omega$. Equation (14) is intended to find the nearest surface point from $\vec{p}$ to the surface of Ω. The largest radius (R_{DM}) of the sphere (S_{DM}) centered at $\vec{p}$ is completely inside the object. The color map expression of the DM is shown in Fig. 4(b). Hilderand and Rüegsegger developed a volume-weighted distance transformation in order to investigate the thickness of objects[42] that is named "Local Thickness (LT)." GPV of LT is defined by the following equation.

$$D_{LT}(\vec{p}) = 2 \max(\{R_{DM}(\vec{x}) | R_{DM}(\vec{x}) > d(\vec{p}, \vec{x}), \vec{x} \in \Omega\}). \quad (15)$$

The equation replaces $R_{DM}(\vec{p})$ by the largest GPV belonging in the same S_{DM}. Hereinafter, it is called the "LT transformation," and the color map expression of the LT transformation is shown in Fig. 4(c). An example of an LT transformation for two-dimensional simple case is shown in Fig. 5. This analysis is calculated using the software *ImageJ*[43] with their plugin for "Local Thickness" analysis[44]. Fig. 5(a) shows a color map of the LT transformation for a ball and stick, and a histogram of the map is shown in Fig. 5(b). It has maxima at 250 and 400 pixels, which correspond to the thickness of the stick and the diameter of the ball, respectively. The LT transformation can be applied to extract the size distribution quantitatively. It is applicable not only for such simple structures, but also for general, complex-shaped objects.

3.1. Pore size distribution analysis of obtained structural model from silica aerogel SAXS data

In order to analyze the constructed model structure based on the SAXS pattern by this LT transformation,

we have defined the following DM whether outside or inside of the n-th primary particle:

$$R_{\mathrm{DM}}(\vec{p}) = \min\left(d(\vec{p}, \vec{r_n}) - R_n\right) \quad (16)$$

where $\vec{r_n}$ and R_n are the position and radius of the n-th primary particle, respectively. When $R_{\mathrm{DM}}(\vec{p})$ is positive, zero or negative, this corresponds to the position $\vec{p}$ being outside, on the surface of, or inside the primary particle, respectively. Then, we can define the LT transformation by the same procedure using equation (15). The actual LT transformation was performed at $300 \times 300 \times 300$ grid points in the case of 300 nm cell size. Fig. 6(a) shows the calculated structural model, and a three-dimensional LT transformed image (color map of pore size) is shown in Fig. 6(b), visualized using the computer program *VESTA*[45]. The histogram of the obtained pore size distribution is shown in Fig. 7. It is noticed that the distribution calculated from a cell size of 100 nm is shifted a little toward a smaller value than those from cell sizes of 200 and 300 nm, as with the graphs of the low-q regime SAXS pattern (Fig. 2(b)) and the density function (Fig. 3).

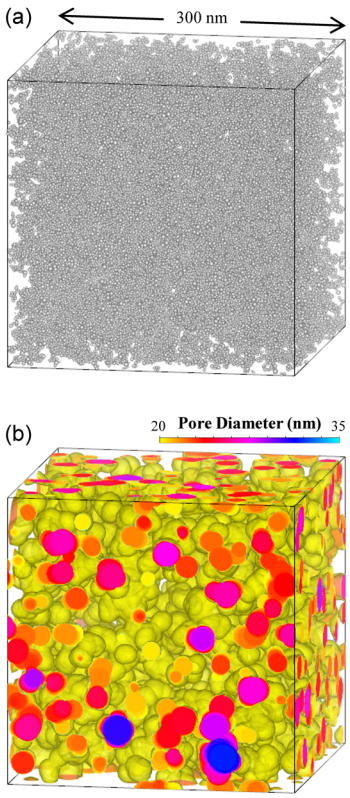

Fig. 6. Different representations of the estimated structure model of the silica aerogel; (a) Particles arrangement in the three-dimensional space, and (b) Pore size distribution.

3.2. Pore size distribution analysis using TEM data

The specimen was tapped and softly ground in a mortar, followed by deposition with ethyl alcohol on a carbon grid, and observed using TEM (JEOL, JEM-2100F(HRPP)). The observed TEM image is compared with a LT transformation image in Fig. 8. To compare pore size distribution of the two-dimensional TEM image to three-dimensional analysis, it is assumed that the area ratio $f_{\mathrm{Map}}(D)$ is converted to volume fraction $f_{\mathrm{Vol}}(D)$ as follows:

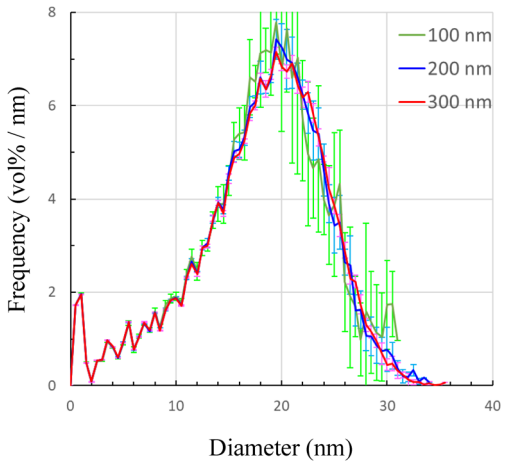

Fig. 7. Histograms of the pore size distribution with cell sizes of 100 nm (green line), 200 nm (blue line) and 300 nm (red line). Each histogram is the mean value calculated from five-times repeating results of the RMC modelling.

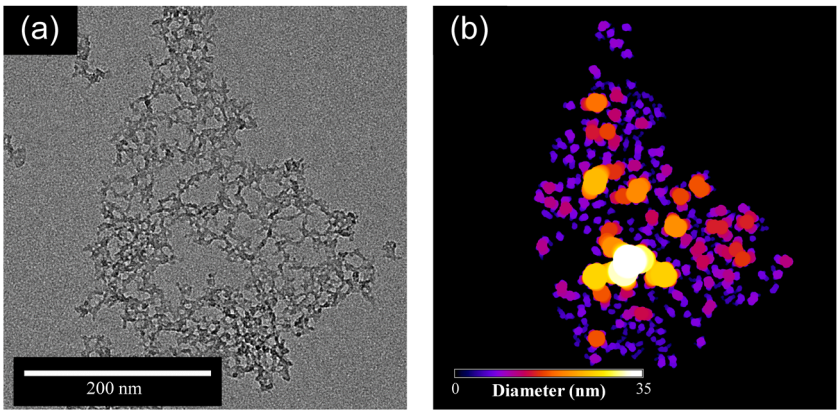

Fig. 8. Comparison of (a) TEM image of the silica aerogel and (b) corresponding pore size distribution.

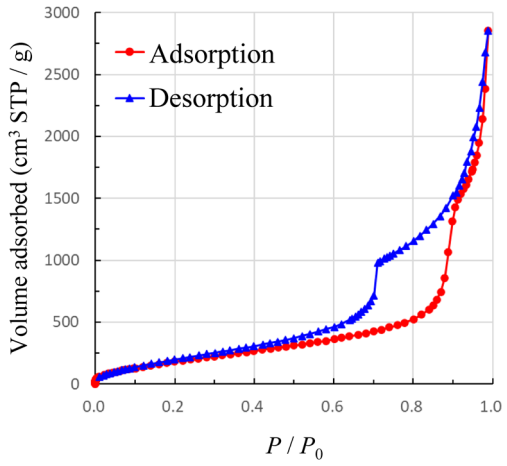

Fig. 9. Nitrogen gas adsorption/desorption isotherms of silica aerogel.

$$f_{\mathrm{Vol}}\left(D_{\mathrm{LT}}\right)=A\left(\frac{\frac{4}{3}\pi\left(D_{\mathrm{LT}}/2\right)^{3}}{\pi\left(D_{\mathrm{LT}}/2\right)^{2}}\right)f_{\mathrm{Map}}\left(D_{\mathrm{LT}}\right), \qquad (17)$$

where A is a normalization constant.

3.3. Pore size distribution analysis by using gas adsorption measurement

First, the sample was outgassed at 423 K for 12 hours under vacuum, then a nitrogen gas adsorption/desorption measurement was performed on Autosorb-iQ from Quantachrome Instruments. According to the IUPAC classification[46], the adsorption/desorption isotherm is a type-IV isotherm, which is associated with mesoporous structures (Fig. 9). The pore size distribution was derived from the adsorption data using the Barrett–Joyner–Halenda (BJH) method[47] and the Non-Local Density Functional Theory (NLDFT) method[48]. The specific surface area s_{BET} (=792 $\mathrm{m^2/g}$) was determined from the multipoint Brunauer–Emmett–Teller (BET) [49] plot. The total volume of open pores, v_{Open} (=4.41 $\mathrm{cm^3/g}$), was directly calculated from the volume of adsorbed nitrogen gas at the highest relative pressure (P/P_0=0.99). Thus, the apparent average pore diameter D_{BET} ($=4v_{\mathrm{Open}}/s_{\mathrm{BET}}$) is 22.3 nm, when all the open pores form a cylinder shape. We calculate each volume fraction, that of particles V_{Particle}, open pores V_{Open}, and closed pores V_{Closed}, by the following equation:

$$\begin{cases} v_{\mathrm{Particle}} : v_{\mathrm{Open}} : v_{\mathrm{Closed}} = V_{\mathrm{Particle}} : V_{\mathrm{Open}} : V_{\mathrm{Closed}} \\ V_{\mathrm{Particle}} + V_{\mathrm{Open}} + V_{\mathrm{Closed}} = 100\,\mathrm{vol\%} \end{cases} \qquad (18)$$

where the lowercase v are the volume per 1 g of the sample. Substitute 1/2.2 into v_{Particle} and 5.6 vol% into V_{Particle}, where 2.2 and 5.6 are the particle density and the particle volume fraction used in the SAXS analysis, respectively. The resultant ratio of $V_{\mathrm{Particle}} : V_{\mathrm{Open}} : V_{\mathrm{Closed}}$ is 5.6 : 54.3 : 40.1. This suggests that over 40 vol% pores in the aerogel are missed using the gas adsorption measurement.

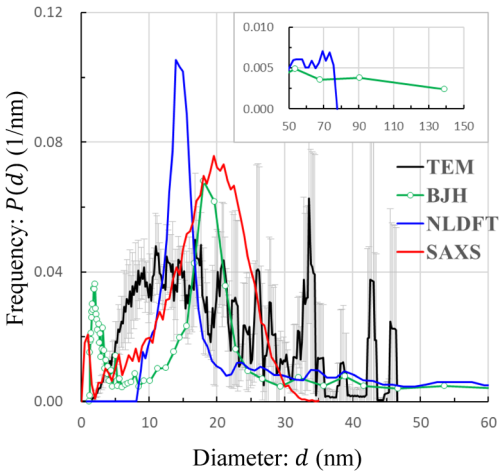

Fig. 10. Comparison of the pore size distributions: TEM (black line) with gray error bars, Gas adsorption (BJH: green line, NLDFT: blue line), SAXS (red line).

Table 1. Comparison of pore size distributions.

	SAXS	TEM*	BJH	NLDFT
Median (nm)	18.9	18.1	22.5	19.7
Mean (nm)	18.0	15.8	9.7	19.8
Mode (nm)	19.5	16.8	18.0	13.9

* TEM's diameters were calculated in the d<30 nm regime.

4. Discussion

Normalized pore size distributions $P(d)$ obtained by SAXS, TEM, and gas adsorption methods, with horizontal axis diameter d, are shown in Fig. 10 and statistical values (median, mean, and mode of diameters) are listed in Table 1. It should be noted that the results of TEM image analysis were calculated in the d<30 nm regime due to the limited field of view in the obtained image. The pore size variations seem to extend over the 30 nm range and show large fluctuation in this region. Regarding the calculated pore size distribution from all TEM images, median, mean and mode values are 18.1 nm, 20.4 nm and 42.6 nm, respectively. Even considering this uncertainty in the TEM results, the obtained median diameters are in good agreement with each other, except for the result of the BJH method. It is slightly bigger than the others and agrees with the average pore diameter D_{BET} (=22.3 nm). On the other hand, the mean diameter of BJH is remarkably smaller than those of the others, because their distribution profile has a peak around 2 nm. However, it is known that the BJH method is less reliable for such small pore analysis, and the mean diameter is calculated as 19.8 nm, if we ignore the "less than 5 nm" region. This agrees with the SAXS and NLDFT results. On the other hand, the mean diameter from TEM is relatively smaller than the others. This may be because smaller pores (less than 10 nm) might remain after sample pulverization.

5. Conclusion

We have introduced an RMC modeling method based on SAXS patterns in order to build a three-dimensional aggregated structure composed of a set of primary particles, and successfully simulated a three-dimensional structure of silica aerogel[19]. Pore size distribution analysis from the obtained structure model is also presented using DM and LT transformation. The result is compared with that of TEM and nitrogen gas adsorption data, and the obtained median diameters are reasonably consistent with each other. To perform SAXS measurements, special sample preparation is not required, so the hierarchical structure of sample materials can be retained as is, even for samples made from the soft materials. The next challenges are to simulate physical properties of the materials; *e.g.,* permeability of the materials, based on SAXS-RMC modeling and performing direct comparison with physical experiments.

References

(1) K. Kakinuma, Y. Chino, Y. Senoo, M. Uchida, T. Kamino, H. Uchida, S. Deki and M. Watanabe: *Electrochim. Acta*, **110** (2013), 316–324.

(2) Y. Senoo, K. Kakinuma, M. Uchida, H. Uchida, S. Deki and M. Watanabe: *RSC Adv.*, **4** (2014), 32180–32188.

(3) C. Huo, X. Tian, C. Chen, J. Zhang, Y. Nan, Q. Zhong, X. Huang, J. Hu and D. Li: *J. Euro. Ceram. Soc.*, **41** (2021), 4231–4241.

(4) V. K. Thakur, M. K. Thakur and A. Pappu: *Hybrid Polymer Composite Materials*, Elsevier (2017).

(5) H. Sugimori, T. Nishi and H. Jinnai: *Macromolecules*, **38** (2005), 10226–10233.

(6) Y. Ikeda, A. Katoh, J. Shimanuki and S. Kohjiya: *Macromol. Rapid Commun*., **25** (2004), 1186–1190.

(7) S. Kohjiya, A. Katoh, T. Suda, J. Shimanuki and Y. Ikeda: *Polymer*, **47** (2006), 3298–3301.

(8) A. Khan, M. Ansari, A. Khan and A. Asiri: *Advances in Aerogel Composites for Environmental Remediation*, Elsevier (2021).

(9) A. Guinier and G. Fournet: *Small Angle Scattering of X-rays*, New York, John Wiley and Sons (1955).

(10) A. Hasmy, E. Anglaret, M. Foret and J. Pelous, R. Jullien: *Phys. Rev. B*, **50** (1994), 6006–6016.

(11) A. Hasmy and R. Jullien: *J. Non-Cryst. Solids*, **186** (1994), 342–348.

(12) R. L. McGreevy and L. Pusztai: *Mol. Simul*., **1** (1988), 359–367.

(13) D. A. Keen and R. L. McGreevy: *Nature*, **344** (1990), 423–425.

(14) B. E. Warren: *X-ray Diffraction*, Dover Publications, New York (1990), pp. 116–149.

(15) P. Debye: *Ann. Phys.*, **351** (1915), 809–823.

(16) P. Scardi, S. J. L. Billinge, R. Neder and A. Cervellino: *Acta Crystallogr*., **A72** (2016), 589–590.

(17) K. Hagita, T. Arai, M. Inui, K. Matsuda and K. Tamura: *J. Appl. Crystallogr*., **40** (2007), s544–s548.

(18) K. Hagita, T. Tominaga, T. Hatazoe, H. Sone, H. Morita and H. Takano：*Nippon Gomu Kyokaishi Jpn*, **89** (2016), 199–204. https://doi.org/10.2324/gomu.89.199

(19) K. Omote and T. Iwata: *J. Appl. Crystallogr*., **54** (2021), 1290–1297. https://doi.org/10.1107/S1600576721006701

(20) S. Alwin and X. S. Shajan: *Mater. Renew. Sustain. Energy*, **9** (2020) 7. https://doi.org/10.1007/s40243-020-00168-4

(21) A. Bisson, A. Rigacci, D. Lecomte and P. Achard: *J. Non-Crystalline Solids*, **350** (2004), 379–384.

(22) K. Tajiri: *J. Surface Science Soc*. *Jpn*, **14**(1993), 546–549. https://doi.org/10.1380/jsssj.14.546

(23) Y. F. Han, X. L. Xia, H. P. Tan and H.D. Liu: *Physica B Condens. Matter.*, **420** (2013), 58–63.

(24) Z. Y. Li, C. Y. Zhu and X. P. Zhao: *Int. J. Heat Mass Transf*., **108** (2017), 1982–1990.

(25) C. Y. Zhu, Z. Y. Li and W. Q. Tao: *J. Heat Transfer.*, **139** (2017), 052405.

(26) X. P. Zhao, Z. Y. Li, H. Liu and W. Q. Tao: *J. Nanosci. Nanotechnol*., **15** (2015), 3299–3304.

(27) C. Y. Zhu, Z. Y. Li, H. Q. Pang and N. Pan: *Int. J. Heat Mass Transf.*, **131** (2019), 217–225.

(28) Z. G. Qu, Y. D. Fu, Y. Liu and L. Zhou: *Appl. Therm. Eng*., **132** (2018), 730–739.

(29) W. Z. Fang, H. Zhang, L. Chen and W. Q. Tao: *Appl. Therm. Eng*., **115** (2017), 1277–1286.

(30) K. Kanamori, K. Nakanishi and T. Hanada: *J. Ceram. Soc. Jpn*, **117** (2009), 1333–1338.

(31) C. M. Wu and S. Y. Lin: *Trans. Mater. Res. Soc. Jpn*, **37** (2012), 123–126.

(32) G. Beaucage: *J. Appl. Crystallogr.*, **29** (1996), 134–146.

(33) H. Grigoriew, D. Chmielewska and J. Gronkowski: *J. Phys. Conf. Ser*., **100** (2008), 052083.

(34) H. Grigoriew, and J. Gronkowski: *J. Non-Cryst. Solids*, **352** (2006), 5492–5497.

(35) K. Omote, Y. Takeda, R. Hirose and J. D. Ferrara: *Rigaku Journal*, **33**(1) (2017), 4–9.

(36) D. Kalasová, T. Zikmund, L. Pína, Y. Takeda, M. Horváth, K. Omote and J. Kaiser: *IEEE Trans. Instrum. Meas*., **69** (2020), 1170–1178. https://doi.org/10.1109/TIM.2019.2910338

(37) R. Tominaga, Y. Nishimura, Y. Suzuki, Y. Takeda, M. Kotera and A. Matsumoto: *Scientific Rep.*, **11** (2021), 1431. https://doi.org/10.1038/s41598-021-80978-2

(38) N. Sakata, Y. Takeda, M. Kotera, Y. Suzuki and A. Matsumoto: *Langmuir*, **36**(37) (2020), 10923–10932. https://doi.org/10.1021/acs.langmuir.0c01481

(39) N. Kunishima, Y. Takeda, R. Hirose, D. Kalasová, J. Šalplachta and K. Omote: *Plant Methods*, **16**(2020) 7. https://doi.org/10.1186/s13007-020-0557-y

(40) P. E. Danielsson: *Comput. Graphics Image Process.*, **14** (1980), 227–248.

(41) J. Serra: *Image Analysis and Mathematical Morphology*, Vol. 2, Academic Press, London (1988).

(42) T. Hildebrand and P. Rüesgsegger: *J. Microsc.*, **185**(1996), 67–75.

(43) C. A. Schneider, W. S. Rasband and K. W. Eliceiri: *Nat. Methods*, **9** (2012), 671–675.

(44) R. P. Dougherty and K. H. Kunzelmann: *Microsc. Microanal.,* **13** (Suppl 2) (2007), 1678–1679.

(45) K. Momma and F. Izumi: *J. Appl. Crystallogr*., **44**(2011), 1272–1276.

(46) K. S. W. Sing, D. H. Everett, R. A. W. Haul, L. Moscou, R. A. Pierotti, J. Rouquérol and T. Siemieniewska: *Pure Appl. Chem.*, **57** (1985), 603–619.

(47) E. P. Barrett, L. G. Joyner and P. P. Halenda: *J. Am. Chem. Soc.*, **73** (1951), 373–380.

(48) P. I. Ravikovitch, S. C. O. Domhnaill, A. V. Neimark, F. Schüth and K. K. Unger: *Langmuir*, **11** (1995), 4765–4772.

(49) S. Brunauer, P. Emmett and E. Teller: *J. Am. Chem. Soc.*, **60** (1938), 309–319.